submitted to *Geophys. J. Int.*

Tracking Aftershock Sequences Using Empirical Matched Field Processing

T. Kværna[1], D. B. Harris[2], S. P. Näsholm[1,3], A. Köhler[1], and S. J. Gibbons[1,4]

[1] *NORSAR, P.O. Box 53, 2027 Kjeller, Norway,*

E-mail: tormod@norsar.no

[2] *Deschutes Signal Processing LLC, Maupin, Oregon, U.S.A.,*

[3] *Department of Informatics, University of Oslo, Oslo, Norway,*

[4] *Norges Geotekniske Institutt (NGI), Sognsveien 72, 0855 Oslo, Norway.*

SUMMARY

Extensive aftershock sequences present a significant problem to seismological data centers attempting to produce near real-time comprehensive seismic event bulletins. An elevated number of events to process and poorer performance of automatic phase association algorithms can lead to large delays in processing and a greatly increased human workload. Global monitoring is often performed using seismic array stations at considerable distances from the events involved. Empirical Matched Field Processing (EMFP) is a narrow frequency band array signal processing technique that recognizes the inter-sensor phase and amplitude relations associated with wavefronts approaching a sensor array from a given direction. We demonstrate that EMFP, using a template obtained from the first P-arrival from the mainshock alone, can efficiently detect and identify P-arrivals on that array from subsequent events in the aftershock zone with exceptionally few false alarms (signals from other sources). The empirical wavefield template encodes all the narrowband phase and amplitude relations observed for the mainshock signal. These relations are also often

robust and repeatable characteristics of signals from nearby events. The EMFP detection statistic compares the phase and amplitude relations at a given time in the incoming data-stream with those for the template and is sensitive to very short-duration signals with the required characteristics. Significant deviations from the plane-wavefront model that typically degrade the performance of standard beamforming techniques can enhance signal characterization using EMFP. Waveform correlation techniques typically perform poorly for aftershocks from large earthquakes due to the distances between hypocenters and the wide range of event magnitudes and source mechanisms. EMFP on remote seismic arrays mitigates these difficulties; the narrowband nature of the procedure makes arrival identification less sensitive to the signals' temporal form and spectral content. The empirical steering vectors derived for the main shock P-arrival can reduce the frequency-dependency of the slowness vector estimates. This property helps us to automatically screen out arrivals from outside of the aftershock zone. Standard array processing pipelines could be enhanced by including both plane-wave and empirical matched field steering vectors. This would maintain present capability for the plane-wave steering vectors and provide increased sensitivity and resolution for those sources for which we have empirical calibrations.

Key words: Earthquake monitoring and test-ban treaty verification; Time-series analysis; Body waves

1 INTRODUCTION

The task of compiling near real-time global seismic event bulletins becomes significantly more difficult during extensive aftershock sequences following large earthquakes. The difficulties extend beyond the vast increase in the number of seismic events occurring in a short time duration. The increased number of seismic signals, often combined with the absence or poor quality of detections on key stations, can degrade the performance of phase association (PA) algorithms and the quality of automatic event bulletins. As a result, the workload associated with the subsequent preparation of analyst reviewed bulletins is strongly increased. On regional and local scales, correlation and subspace detectors may be able to categorize entire sequences with a remarkable completeness (e.g. Harris & Dodge 2011; Benz et al. 2015). Globally, Gibbons et al. (2016) suggest that iterative strategies may be needed in which the world-wide PA procedure is performed repeatedly with the input modified on each iteration as the

picture of seismicity becomes more complete. Specifically, it is suggested that events in the aftershock region can be detected and located in the first iteration using a separate process, and that the phase detections associated with these events are removed from the input to the PA algorithm.

This targeted aftershock classification could probably be performed efficiently using pattern detectors or grid-search methods over dense local and regional seismic networks (e.g. Tang et al. 2014), but may be challenging given only a sparse global network. Considering specifically the seismic network of the International Monitoring System (IMS), for monitoring compliance with the Comprehensive Nuclear-Test-Ban Treaty (CTBT), we note that the network is dominated by array stations. Arrays provide enhanced information about individual signal detections and wavefronts, exploiting measurements of phase- or time-shifts between signals recorded on closely-spaced sensors. We here seek to explore the limits of how seismicity in a given source region can be characterized by distant arrays using advanced signal processing.

Fig. 1 displays a dayplot of the data from a short-period vertical motion seismometer at one site of the Karatau array (KKAR) in southern Kazakhstan at several hundred kilometers distance from the Kashmir earthquake on October 8, 2005. This array is part of the observational network operated by the Institute of Geophysical Research of the National Nuclear Center of the Republic of Kazakhstan. Each signal arrival that is confidently identified as a first Pn onset from the aftershock region, based upon array analysis, is marked with a red filled circle. At this distance of about 900 km, around 100 s separate the Pn and Sn arrivals. The duration of the KKAR wavetrain from a single Kashmir earthquake can exceed 3 minutes from first Pn arrival to the end of the S-wave coda, and there are many occasions during this day when Pn arrivals from multiple events will be recorded within such a time span. Note that the Lg phase that often dominates regional signals along continental propagation paths is not observed at this station from this source region (see e.g. Sanborn & Cormier 2018, and references therein). Many of the apparent gaps in Pn detections (red symbols) in Fig. 1 correspond to the wavetrains from the larger earthquakes, and it is very likely that the signals from smaller earthquakes in these intervals are simply masked by the coda.

Fig. 2 displays waveform segments and the corresponding signal and noise spectra for three earthquakes in the Kashmir sequence. The first event is the magnitude 7.6 mainshock, for which the signal is emergent but obtains high amplitudes. The signal and noise spectra (Fig. 2 c) show that the energy following the signal arrival greatly exceeds the energy in the background noise over the full frequency range of this short-period seismometer. The second event displayed is a magnitude 5.4 aftershock. The regional signals are recorded with a high signal-to-noise ratio (SNR), even in the raw data, and the earthquake is well-recorded teleseismically. The maximum SNR is at around 2 Hz (Fig. 2 d). The third event is a magnitude 4 aftershock that is not visible in the raw data and is only recorded

with a satisfactory SNR above 3-4 Hz (Fig. 2 e). The duration of this third signal is far shorter than for the larger earthquakes, with only a direct arrival visible. Slinkard et al. (2013) demonstrated that this particular aftershock sequence had very few pairs of events with similar waveforms, such that waveform correlation would make a poor classifier identifying aftershocks belonging to the sequence. The waveform dissimilarity quantified by Slinkard et al. (2013) is clear in Fig. 2.

The noise spectra (the shaded regions) in Fig. 2 highlight another of the challenges in seismic monitoring of aftershocks. The first Pn arrival from the mainshock rises from quiet, ambient, background noise, but the aftershock Pn arrivals emerge from a much higher noise level comprising coda wave energy from previous earthquakes in the sequence. If we were to plot the signal spectrum for aftershock 2 (Fig. 2 e) with the noise spectrum for the mainshock (Fig. 2 c) it is clear that this magnitude 4 earthquake would be detected with a high SNR over a broad frequency range under normal background noise conditions. The wavetrains of preceding aftershocks reduce both the SNR and the frequency band in which SNR is sufficient for confident detection. The frequencies at which signal coherence between sensors is strongest, and at which classical array processing performs best (typically between 1 and 4 Hz on an array with the dimensions of the KKAR station), are also the frequencies where the coda noise is strongest. A key to confident identification of signal arrivals in increased noise may be a method that extends coherent array processing to higher frequencies at which the level of coda noise is lower (see also, e.g., Kværna et al. 2021).

Harris & Kværna (2010) describe the application of Empirical Matched Field Processing (EMFP) on a small aperture seismic array for classification of seismic arrivals generated by closely spaced mining explosions. EMFP recognizes characteristics in the seismic wavefronts arriving at closely spaced sensors from a given region. The EMFP fingerprint corresponding to a seismic arrival in the array traces is closely related to the (frequency-dependent) move-out in time of the signals across the array. These characteristics are determined both by the source location and by properties of the path, all the way from source to receiver. The deviation of the observed wavefront from the predicted far-field plane-wavefront increases with increasing frequency. This is because the form of higher frequency signals is affected more by scattering and diffraction on heterogeneities of smaller length scales. Such deformations of the ideal wavefront degrade the performance of classical beamforming but are indeed exploited by EMFP to obtain the best characterization of a wavefront from a given source region. It has been demonstrated (e.g. Wang et al. 2015) that EMFP as a pattern detector can reduce detection thresholds for low magnitude seismicity recorded on a local network. The application in Harris & Kværna (2010) was assigning a source to ripple-fired mining explosions, the different source-time functions in the signals typically precluding the effective use of waveform correlation. The narrowband nature of EMFP mitigated this problem since the phase and amplitude relations between sensors in the array in each frequency band

are relatively insensitive to the temporal nature of the signal. Köhler et al. (2022) exploited the same properties of the narrowband formulation to detect the occurrence of signals from glacial calving events in array data. Even if the events originated from the same glacier, the signals differed significantly because of differences in the source-time function. Thus, waveform correlation methods were found to be unsuitable for detection of these calving events. In this paper, we demonstrate how properties of the narrowband EMFP formulation can provide enhanced characterization of aftershock sequences using EMFP templates from P-arrivals from the mainshocks only. This monitoring situation has very different challenges to the glacial calving study: the geographical extent of the source region, the short duration of the arrivals, and the vast range of amplitudes and spectral shapes that need to be covered.

Signal pattern detectors (correlation and subspace detectors) recognize familiar waveform shapes and usually perform best when using the full wavetrain and a high time-bandwidth product (TBP). Detectors searching for transient signals of unknown form, without a priori knowledge of the fine signal structure, usually identify changes in the waveform properties (e.g., amplitude, frequency content) over time-windows of the order of only a few seconds. We apply a form of EMFP here as a bridge between these two categories of detectors, to identify rapid changes in the incoming wavefield that have fine-structure consistent with previously observed signals. In Sec. 2 we examine the structure of wavefronts arriving on an array station from an intensive aftershock sequence and explore how properties of these wavefronts can be exploited in a matched field detection framework. In Sec. 3 we sketch a framework for robust detection of arrivals from aftershocks using only the spatial fingerprint of the first arrival from the mainshock and, in Sec. 4, we discuss considerations in applying the methods to networks of arrays and more general processing pipelines.

2 EXPLOITATION OF WAVEFRONT PROPERTIES FOR IMPROVED DETECTION AND ESTIMATION

To make the most complete and accurate inventory of aftershocks possible following a large earthquake, we want a process that detects and identifies every arrival from the aftershock region on a network of seismic stations. This network will probably be a significant subset of our global monitoring network: those stations with the best detection capability for the source region in question. We want to detect as many aftershock arrivals as possible within the elevated noise levels following the mainshock and, at the same time, make sure that we eliminate all signals that do not come from this source region from this event-specific process. The process should be optimal for the kind of seismic stations that dominate our monitoring network; for the IMS, this means seismic arrays with apertures of a few km. Since the process is to act following a first arrival from the mainshock, it would be beneficial if we could exploit

specifically the form of the mainshock signal to enhance the detection capability for aftershocks. In this section, we outline the basis for selecting EMFP as an ideal method for this purpose.

Fig. 3 shows the locations of the 2005 Kashmir earthquake and its aftershocks (Gibbons & Kværna 2017). Over 100 km separates the most distant aftershocks in the cluster, although even these distances are relatively small in comparison with the approximately 900 km to the KKAR (Karatau) array in Kazakhstan. The array is approximately 4 km in diameter and the great circle backazimuth from receiver to source varies from between 157 and 167 degrees for the events displayed. The distances between events, compounded by the tectonic complexity of the source region and wide range of focal mechanisms (e.g. Butler 2019), together with the high frequencies at which the signals are observed, result in waveforms that are insufficiently similar over the source region for good performance by correlation detectors (Slinkard et al. 2013). The accuracy with which the array can measure the Direction of Arrival (DOA) or backazimuth using standard procedures is not sufficient to differentiate between different parts of this source region. The resolution is not only limited by the Rayleigh criterion but also by frequency-dependent biases in the backazimuth and slowness estimates with respect to their theoretical values given by standard velocity models (e.g. Kværna & Doornbos 1991). The reduced Pn signal coherence between signals on the KKAR sensors at higher frequencies (see Ringdal et al. 2009) also imposes constraints on the frequency range usable for coherent array processing. Given the signal and noise spectra (Fig. 2), we are restricted to frequencies between around 1 Hz and 5 Hz. The 2-4 Hz band provides the best capability given low SNR below 2 Hz for the smaller events and diminished signal coherence above 4 Hz. Harris & Kværna (2010) demonstrate how the frequency range amenable to coherent processing is increased using empirical signal processing in narrow frequency bands, since the need to satisfy uniform time-delays and perfect coherence for all frequencies, at all sensors, is removed.

Fig. 4 displays narrowband slowness beam power grids for the Pn wavefronts crossing the KKAR array for the three earthquake signals displayed in Fig. 2. For a given short data-window starting at time t, and frequency ω, the panels in Fig. 4 display relative power as a function of slowness, $\boldsymbol{s}$,

$$\hat{P}(t,\omega,\boldsymbol{s}) = \frac{\boldsymbol{\varepsilon}(\omega,\boldsymbol{s})^H \boldsymbol{R}(t,\omega)\boldsymbol{\varepsilon}(\omega,\boldsymbol{s})}{tr\left\{\boldsymbol{R}(t,\omega)\right\}} \tag{1}$$

where H denotes the Hermitian transpose and the plane-wave steering vectors $\boldsymbol{\varepsilon}(\omega,\boldsymbol{s})$ are given by

$$\boldsymbol{\varepsilon}(\omega,\boldsymbol{s}) = \left[e^{-i\omega\boldsymbol{s}.\boldsymbol{x}_1} \quad \ldots \quad e^{-i\omega\boldsymbol{s}.\boldsymbol{x}_N}\right]^T \tag{2}$$

with $\boldsymbol{x}_i$ denoting the N sensor locations. The narrowband N by N spatial covariance matrices, $\boldsymbol{R}(t,\omega)$, (see Johnson & Dudgeon 1993) are calculated using the multitaper coherence routines of Prieto et al. (2009) on short windows, typically 3 or 4 s long, starting at time t (see Gibbons et al. 2017, for details). The multitaper routines provide very stable estimates of the phase differences between signals over

short time-windows, mitigating the spectral leakage issues that can make narrowband $f-k$ estimates less stable than broadband estimates when standard Fast Fourier Transform approaches are applied.

For each Pn arrival in Fig. 4, the optimal slowness vector at 2 Hz (left) is significantly different from the optimal slowness vector at 4 Hz (right). For each event, the apparent velocity ($v_{\rm app}$) for the 2 Hz estimate is slower than 8 km/s whereas $v_{\rm app}$ for the 4 Hz estimate is faster than 10 km/s. This is a qualitative difference since the slower apparent velocity would usually identify the arrival as a Pn- or Pg-phase from regional distances whereas the faster apparent velocity is indicative of a teleseismic or far-regional P-arrival. Broadband estimates of the slowness vector are made by summing the narrowband frequency-wavenumber spectra (the grids as displayed in Fig. 4). There are many different ways in which this summation over frequencies can be performed. One alternative, the simplest, is to stack all of the narrowband grids with each grid weighted equally. Alternatively, different weights could be applied to the different grids, either determined beforehand or calculated in some way based on properties of the data. In this study, we consider only uniformly weighted grid summations. Broadband estimates result in a scatter consistent with the narrowband patterns in Fig. 4, with the precise backazimuth and $v_{\rm app}$ measured depending upon the quality of the estimates at each frequency. Different results may be anticipated if different weightings were to be applied to the grids.

There is a striking similarity between the narrowband slowness grids of the Fig. 4 events, especially given the different waveform and spectral characteristics (Fig. 2). The lowest SNR signal shows a weaker relative power than the higher SNR signal, although the mainlobe and sidelobe structures are similar between events. The temporal waveforms vary greatly between the Fig. 2 events, limiting the viability of correlation detectors. The narrowband grid similarity between events suggests a fingerprint that can be used to identify subsequent arrivals. The 2 Hz and 4 Hz slowness grids indicate very different patterns, suggesting that the narrowband phase relations contain a richer wavefront description than a plane-wave parametrization. How reliable is this signature in identifying aftershock sequence arrivals? Is it so specific to a single source location that it will fail to recognize aftershocks further from the mainshock, or is it so general that it will trigger on any wavefront arriving from the same general direction?

Assuming that the array traces corresponding to a seismic arrival gives the following spatial covariance matrix estimate at time t_0:

$$\boldsymbol{R}_0(\omega) = \boldsymbol{R}(t_0, \omega), \tag{3}$$

the principal eigenvector of $\boldsymbol{R}_0(\omega)$ becomes a complex vector of length N. In our case this reference time, t_0, is the onset of the first P-wave from the mainshock, and we wish to compare the form of the arriving wavefront at a given time t with the form of the arriving wavefront at the reference time, t_0. Fig. 5 visualizes the narrowband spatial covariance matrices generated from short segments of waveform data on all array sensors. In panel a), the wavefront satisfies perfectly the plane wavefront

model; that is to say that the synthetic wavelets are identical (perfect coherence) and that the time delays satisfy exactly the relations determined by the sensor locations and the slowness vector of the incoming wavefront. In panel b), the data are real; the signals are not identical and the apparent time delays are a function of frequency and do not fit a plane-wave model exactly. The coloured symbols in the covariance matrix representations in panel a) all have identical size for all frequencies, a consequence of the perfect coherence. The symbol sizes in the covariance matrix representations in panel b) diminish in size as the frequency increases, a consequence of the reduced waveform similarity. At the lowest frequencies the observed phase shifts closely resemble the theoretical phase shifts, although there are notable differences. At higher frequencies, the differences in phase shift for given channel combinations increase. Also displayed in Fig. 5 are the principal eigenvectors of the covariance matrices. The principal eigenvectors in panel a) are the theoretical steering vectors, $\boldsymbol{\varepsilon}(\omega, \boldsymbol{s})$, defined by the plane-wave model delay-times. The principal eigenvectors in panel b) are the empirical steering vectors, $\boldsymbol{\varepsilon}_0(\omega) = \boldsymbol{\varepsilon}_0(t_0, \omega)$. Both the covariance matrices and principal eigenvectors displayed in Fig. 5 synthesize array data properties that represent the impinging waves. These matrices and vectors describe the inter-sensor array data similarity structure and have different, and potentially more repeatable, characteristics of the wavefront structure than the temporal evolution of the waveform recordings themselves.

Just as $\hat{P}(t, \omega, \boldsymbol{s})$ in Eq. 1 provides a measure of the energy incident on the array consistent with the plane-wavefront hypothesis, $\boldsymbol{s}$,

$$\hat{P}_0(t, \omega) = \frac{\boldsymbol{\varepsilon}_0(\omega)^H \boldsymbol{R}(t, \omega) \boldsymbol{\varepsilon}_0(\omega)}{tr\left\{\boldsymbol{R}(t, \omega)\right\}} \tag{4}$$

provides a measure of the energy incident on the array consistent with the so-called empirical steering vector, $\boldsymbol{\varepsilon}_0(\omega)$. Harris & Kværna (2010) demonstrate how the empirical steering vectors derived from events at a template location capture more of the energy from subsequent co-located events than the optimal plane-wave sterring vectors. This is to say that deviations from the plane-wave models ($\boldsymbol{s}$), observed in the real-world wavefronts, are captured by the empirical steering vectors.

We can form a measure

$$\hat{P}_0(t, \omega, \boldsymbol{s}') = \frac{\left[\boldsymbol{\varepsilon}(\omega, \boldsymbol{s}') \circ \varepsilon_0(\omega)\right]^H \boldsymbol{R}(t, \omega) \left[\boldsymbol{\varepsilon}(\omega, \boldsymbol{s}') \circ \varepsilon_0(\omega)\right]}{tr\left\{\boldsymbol{R}(t, \omega)\right\}} \tag{5}$$

where we consider a plane-wavefront vector perturbation, $\boldsymbol{s}'$, imposed upon the empirical phase shifts, $\varepsilon_0(\omega)$. $[\boldsymbol{a} \circ \boldsymbol{b}]$ denotes the Hadamard (element-wise) product between the complex vectors $\boldsymbol{a}$ and $\boldsymbol{b}$ with

$$[\boldsymbol{a} \circ \boldsymbol{b}]_j = a_j b_j. \tag{6}$$

Fig. 6 displays the narrowband beam power slowness grids (Eq. 5) evaluated for the Pn arrivals for aftershocks 1 and 2 for the perturbation vector

$$\boldsymbol{s}' = (s'_x, s'_y) \tag{7}$$

when the empirical steering vector for the mainshock Pn arrival is imposed. In Fig. 4, with no imposed empirical steering vector we saw a qualitative difference between the directions from which the wavefield appears to approach the array at 2 Hz and at 4 Hz. In Fig. 6, the maximum beam power is approximately centered for both aftershock arrivals at both frequencies. We can exploit this result to screen out false alarms, identifying any detected signals that are not P-wave arrivals from within the aftershock zone. If we perform f-k analysis on a detected signal with the empirical steering vector from the mainshock imposed, and a clear non-zero slowness vector is measured, the signal can be assumed to be unrelated to our aftershock sequence.

Having confirmed the stability of the steering vectors of a typical Pn arrival from the aftershock sequence, from one event to another, we need to devise a detection framework that reports most reliably when, and only when, a wavefront from this same source region is detected. The estimates of the covariance matrices are measured in short time-windows (compared with, say, the full duration of the wavetrain) and we seek a process which interrogates the waveforms continuously to find a characteristic set of phase shifts in the incoming datastream. If $\boldsymbol{x}_i$ and $\boldsymbol{x}_j$ denote the position vectors of stations i and j in our seismic array then the set of locations $\boldsymbol{x}_{ij}$ given by

$$\boldsymbol{x}_{ij} = \boldsymbol{x}_j - \boldsymbol{x}_i \tag{8}$$

define the so-called co-array (see also, e.g. Johnson & Dudgeon 1993, Chapter 3 for an explanation of the co-array concept in array signal processing). The elements R_{ij} of the covariance matrices $\boldsymbol{R}$ displayed in Fig. 5 can also be drawn as a function of the location $\boldsymbol{x}_{ij}$ of the corresponding element in the co-array. Fig. 7 displays the phase differences and coherence measures as a function of position in the co-array. The theoretical "bubble plot" for 2 Hz (top left) shows bands in the phase differences tilted in the direction of arrival with the band spacing dictated by the sensor geometry, the apparent velocity, and the wavelength. The corresponding theoretical phase shift bands at 4 Hz (lower left) have the same angle but are narrower due to the shorter wavelength. The remaining panels in Fig. 7 are measured from the data at the time of the Pn arrivals for the three events displayed in Fig. 4. Although the properties of the wavefronts are more easily interpreted in the narrowband slowness plots in Fig. 4, we can make predictions about the wavefront behaviour from observing these phase and coherence relations. For the 2 Hz bubble plots, the measured banded patterns are very close to the theoretical patterns but with a perceptible change in the angle (also visible as an azimuth deviation in the left-hand panels of Fig. 4). For the 4 Hz bubble plots, the measured bands are wider than for the theoretical patterns (also visible as an increase in the apparent velocity in the left-hand panels of Fig. 4). The size of the symbols in the theoretical bubble plots are identical (perfect signal coherence assumed). The size of symbols for the empirical bubble plots are diminished as the signal coherence decreases. For aftershock 1, the diminishing coherence is most notable at 4 Hz as a result of the increased wavefield

scattering at the smaller length scale. For aftershock 2, the diminishing coherence is even more acute at 2 Hz: a result of reduced SNR.

The differences between the phase and coherence patterns between the theoretical expectations and the measurements allow us to evaluate the deformation of the wavefront on the various sensors as a function of frequency. In each panel of Fig. 7 is a square containing two very closely spaced elements of the co-array; i.e. two pairs of sensors with very similar relative positions. For the theoretical patterns (left) the two symbols in the square have very similar colours, reflecting the very similar time delays that should take place between the sensors in each of the pairs. For the empirically measured phase shifts, the colours of the two symbols in the square are very different, meaning that the wavefront has used different time intervals to cover the same horizontal distance in different parts of the array. A way to visualize a matched field detector is a pattern detector which compares the set of phase shifts (coloured symbols in Fig. 7) with either a theoretical set of phase shifts or a measured set of phase shifts. It is the latter of these cases that is referred to as Empirical Matched Field Processing or EMFP.

3 ANATOMY OF A MATCHED FIELD DETECTOR

Our results from single Pn phase observations demonstrate that the empirical matched field representation is consistent for first arrivals from different events in the aftershock region with very different characteristics (e.g., spectral content and SNR). We wish to use the similarity between the narrowband phase shift pattern in our template and the narrowband phase shifts measured at any given time in the incoming data as a means of detecting the presence of an aftershock arrival. The question is whether a detection statistic that measures this similarity can be a sufficiently reliable indicator of the presence of a signal of interest. In other words, is the EMFP detection statistic evaluated at the times of aftershock arrivals sufficiently greater than the background level, and is the variability of the background level of the detection statistic low enough to be able to set a practical detection threshold? In this section, we explore how to develop a robust detection framework based on EMFP.

In Fig. 8 we sketch the foundations of a detection procedure using matched field statistics calculated in very short, overlapping, time-windows. For a given time-window, we calculate elements R_{ij} of the covariance matrix for traces $i, j \in \{1, ..., N\}$ and distinct frequencies $\omega_k : k \in \{1, ..., K\}$: e.g. using the multitaper coherence routines of Prieto et al. (2009). For our given time, t, we can then calculate K scalar values of the quadratic form $\hat{P}_0(t, \omega)$ (Eq. 4) using our chosen steering vector. Each one of these K values tells us how similar the phase-shifts at this time and this frequency are to the corresponding phase-shifts defined in our empirical steering vector. In the same way that a spectrogram holds power density estimates as a function of time and frequency, we here have a wavefield-similarity metric that is a function of time and frequency. We will here refer to this as a pseudospectrogram so as to remind the

reader of the form of its time and frequency dependence, while simultaneously emphasizing that it is not a conventional spectrogram. We build our pseudospectrogram by repeating this process for each of many overlapping windows. Detecting short-period seismic signals (e.g. between 1 and 5 Hz), on arrays with apertures of several km typically requires time-windows of between 3 and 5 s. This time duration is long enough to estimate the phase and amplitude relations between the signals on the different sensors, but still short enough that stationarity over the data interval is maintained. The sampling density in time of the pseudospectrogram should be sufficient to record changes in the coherence relatively smoothly such that no significant discontinuities are recorded between time-samples. Based on observations of the rate of change of the coherence with a given slowness, 0.5 s is found to be a good sampling interval. More rapid sampling than this increases the computational cost without providing new information.

The uppermost panel in Fig. 9 displays a real-data expression of the pseudospectrogram sketched in Fig. 8. Each pixel displays the value of $\hat{P}_0(t,\omega)$ (as defined in Eq. 4) where t and ω denote the time and frequency respectively. The 0 subscript indicates the application of the empirical steering vector $\boldsymbol{\varepsilon}_0(\omega) = \boldsymbol{\varepsilon}_0(t_0,\omega)$ extracted as the principal eigenvector of the covariance matrix of the Pn-onset at time t_0 for the signal from the mainshock. A 20-minute-long data segment is displayed, containing 3 moderate sized aftershocks in addition to many smaller events. Aftershocks 1 and 2 displayed in the previous figures are the arrivals labelled "A1" and "A2" in Fig. 9, both clearly visible as vertical red bars. The pixels shown at the times of the Sn arrivals are largely blue, indicating that the slowness vector for the Sn-arrival is sufficiently different from the Pn arrival slowness vector to prevent a significant match. This is significant since a classical beam steered with the time delays applicable to the Pn arrival will have a significant burst of energy at the time of Sn; the $\sqrt{N}$ noise reduction will not completely suppress this. The absence of red pixels at the time of this Sn arrival time suggests that Sn-triggers will generally not occur using a detection statistic based upon this $\hat{P}_0(t,\omega)$ measurement.

There are many examples of seismic signal detectors that exploit both time and frequency signatures. Joswig (1990) demonstrates signal identification through pattern matching in the time-frequency space. Taylor et al. (2010) sought short-duration transients on spectrograms that appeared as vertical lines and applied image processing filters optimized for such shapes. A slightly different approach is required when detecting signal onsets in spectrograms from long codas. Gibbons et al. (2008) apply a transformation of the form

$$S(\omega,t) = (\log_{10}[P(\omega)_{t+}] - \log_{10}[P(\omega)_{t-}])\log_{10}[P(\omega)_{t+}] \tag{9}$$

where $P(\omega)_{t+} = P(\omega,t,L)$ denotes the amplitude density spectrum measured for the window immediately following a time t, and $P(\omega)_{t-} = P(\omega,t-L-\boldsymbol{\varepsilon},L)$ the estimate from the window ending at time t. Here L is the window length used to make the measurement and $\boldsymbol{\varepsilon}$ is the shorter separation between the sliding windows $P(\omega)_{t+}$ and $P(\omega)_{t-}$. This transformation is intended to provide local

maxima at times with both high signal amplitude and a high signal amplitude increase. This is necessary given that seismic signals can obtain the greatest amplitudes significantly later than the onset.

The function $\hat{P}_0(t,\omega)$ in Fig. 9 has a rather different form depending on the event size. For the three largest aftershocks, coherent energy consistent with the imposed phase shifts occurs across the full frequency range (1-5 Hz). At the lowest frequencies, the match with the empirical steering vectors persists far into the coda. The match with the Pn-phase shifts ends, over a minute later, with the Sn arrival. At this time, a coherent arrival with a different set of time delays starts to dominate. As the frequency increases, the duration of the high match with the empirical steering vectors decreases until only a short transient at the signal onset matches. For many smaller signals, only a short-duration vertical band is observed, typically only at higher frequencies. Identifying signal arrivals from the pseudospectrogram appears simple for the human eye. A transformation

$$S(\omega,t) = \left(\hat{P}(\omega)_{t+} - \hat{P}(\omega)_{t-}\right) \hat{P}(\omega)_{t+} \tag{10}$$

places strong vertical bars at the signal arrivals and diminishes into the signal coda (Fig. 9, middle panel). Note that the logarithm is required in Eq. 9 since the un-normalized amplitude density spectrum terms $P(\omega,t,L)$ cover a vast range. The relative power terms $\hat{P}$ in Eq. 10 are all between zero and unity and so no logarithm is needed.

We wish to transform a broadband signal with a visible impression in the time-frequency domain to a simple time-series from which triggers are identified reliably. In the lowermost panel of Fig. 9 are simple mean values of the time-frequency grids in the other two panels. The black line is the mean over all frequencies of $\hat{P}_0(t,\omega)$. The curve varies relatively smoothly, and the human eye can identify several of the likely arrivals from the steep discontinuities. The limited dynamic range may make the signals difficult to identify using, for example, a power detector. The orange trace shows the mean over ω of $S(\omega,t)$. The peaks are clearer, but the variability in the noise floor is still high. The difference term in Eq. 10 means that small contributions, in particular from coda energy at the lower frequencies, can lead to an oscillation unrelated to new signal arrivals. The array response for the lower frequencies has a broader peak such that the likelihood of coincidental match of coherent noise energy with the imposed phase shifts is greater at lower frequencies than at high frequencies.

Panels a) and b) of Fig. 10) show single frequency scalar traces selected from the upper two panels of Fig. 9. For a single frequency, ω, $\hat{P}_0(t,\omega)$ is a noisy time-series spanning the interval $[0,1]$. There are many frequencies at which a given arrival fails to provide a significant imprint. It is the consistency of behaviour over a broad range of ω that provides useful signal and allows for enhanced detection through stacking. $S(t,\omega)$ is a less noisy time-series and now spans the range $[-0.25,1]$ with negative values indicating a decrease in $\hat{P}_0(t,\omega)$ from one time-window to the next. A stacking operation over ω may degrade local maxima over some frequency range if there are coincidentally negative values at different

frequencies. Replacing $S(t,\omega)$ with $\exp_{10}S(t,\omega)$ (panel c) provides a function theoretically spanning the range $[0.56, 10]$, but increasing the significance of the local maxima of $S(t,\omega)$. The mean over ω of $\exp_{10}S(t,\omega) - 1.0$ (panel d) finally gives us a scalar time series in which a very limited number of peaks can be identified by setting a simple threshold value.

The trace in Fig. 10 d) can be considered to be the equivalent of a beam output for a single empirical steering vector, $\boldsymbol{\varepsilon}_0(\omega)$. The significance is that it uses only the first few seconds of the signal generated by the mainshock of the earthquake sequence as a template; we do not need to wait for multiple aftershocks to build up a database of templates. It detects more signals than a correlation detector using the mainshock signal as a template (Slinkard et al. 2013) but fewer signals than an STA/LTA detector on a filtered beam (which would, for example, also have detected the Sn arrivals). The procedure performed at each frequency ω is designed to reduce the influence of frequencies at which the signal is not well observed. As Gibbons (2014) points out for detectors using multitaper spectrograms, this detector would be quite stable to strong noise in narrow bands provided that the band affected is small in comparison with the band occupied by the signal.

4 CONSIDERATIONS IN NETWORK PROCESSING AND PHASE ASSOCIATION

The preceding sections have focused only upon the single seismic array KKAR. We will now consider a network monitoring operation, where the aftershock sequence will be observed on seismic arrays, with different geometries and placements, at many different directions and distances. Fig. 11 displays $\hat{P}_0(t,\omega)$ and $S(t,\omega)$ pseudospectrograms for four different seismic arrays. BVAR (Borovoye), WRA (Warramunga), and ILAR (Eielson) are IMS arrays.

The KKAR array is unique among these stations in recording the full regional wavetrain with Pn and Sn with coda. BVAR, ILAR, and WRA record teleseismic P from this sequence with varying lengths of coda-wave energy. The P-arrivals at BVAR typically have high SNR and, while many of the smaller events visible at KKAR are not observed at BVAR, there are a few signals at BVAR not visible at KKAR because of high amplitude S-wave coda. The P-wave coda at BVAR can have quite long duration, even for relatively small events.

The WRA $\hat{P}_0(t,\omega)$ pseudospectrogram shows considerably less red, i.e., high beam power, than for KKAR and BVAR although many of the faint vertical lines generate significant stripes in the $S(t,\omega)$ pseudospectrogram. The bursts of red areas have a shorter duration than at the closer arrays. WRA is a significantly larger array than KKAR and BVAR (aperture exceeding 20 km, as opposed to 5 km). This may lead to a slightly reduced relative power, especially for higher frequencies. However, the reduction in coherence for the background noise is at least as significant as the reduction in coherence for the signal and the WRA noise floor appears to be exceptionally low. WRA also has 20 sensors compared

with the 9 sensors at KKAR and BVAR which also increase the contrast between signal and noise. The larger aperture at WRA means that the peak in the slowness grid for a given frequency is much narrower than at the smaller arrays. Given the much greater distance between the aftershock zone and WRA, the sharpness of the peak in slowness space is less significant than it would have been for KKAR since the same range of backazimuth angles at this greater distance covers a far wider geographical region.

Finally in Fig. 11 is ILAR, Alaska. As for WRA, coherent signals consistent with the first arrival phase shifts of the mainshock are of short duration. Although marginally closer to Kashmir than WRA, ILAR appears to have the poorest sensitivity to aftershock zone events. While WRA records energy from these events at frequencies above 4 Hz, ILAR appears to be limited to frequencies up to 3 Hz.

There are many considerations in the definition of the matched field templates used in this study. Window length, frequency band, and sampling interval for the pseudospectrams are key questions to be addressed, although we note that a good knowledge of the signal and noise spectra is beneficial for any form of targeted signal processing.

Fig. 12 displays four different traces targeting Pn arrivals at KKAR from the Kashmir aftershock sequence. Panel a) displays the filtered Pn-beam as would be applied in a classical plane-wave beam deployment. Although optimized for the best-fitting plane-wave Pn time delays from the main shock, it is clear that several signals with different slowness vectors would also record a high SNR. A further problem (c.f. Fig. 4) is that the time delays predicted for this arrival do not correspond exactly to the phase shifts valid for the different frequency bands; the differences between e.g. 2 and 4 Hz mean that no set of time delays will perfectly define the correct phase shifts. Smaller events are seen only at higher frequencies and, given the shorter wavelength, these waveforms are more diminished by beamforming misalignment.

Panel b) shows the AR-AIC trace discussed by Gibbons et al. (2016). This trace is calculated from the beam displayed in panel a). An advantage of this trace is that the times of the local maxima provide exceptionally good estimates of the signal onset time. The trace has a lower dynamic range than the beam itself and it is easier to identify at a glance arrivals from the smaller events than from the original waveforms. Since the AR-AIC trace is calculated purely from auto-regressive models of segments of the beam, it is also unable to differentiate between the signals of interest and unrelated signals.

Panel c) displays two matched field scalar traces as developed in the previous section. In the first, labelled “Plane-Wave Matched Field Scalar Function”, we have used the steering vector generated using the plane-wave model time-delays, the same as used for the beam in a) (c.f. Fig. 5 a). In the second, labelled “Empirical Matched Field Scalar Function”, we have used the empirical steering vector generated using the P-wave arrival from the mainshock signal (c.f. Fig. 5 b). Both of these traces have an even lower dynamic range than the AR-AIC trace, but far lower noise floors. The matched field

scalar traces are only sensitive to first Pn-arrivals from the source region and, unlike the AR-AIC trace, do not generate a trigger at the time of the Sn-arrivals. These traces are sampled more coarsely than the AR-AIC trace and have the same sampling interval used for constructing the pseudospectrograms. Again, there is little to be gained by using a shorter sampling interval. The need for a short sampling interval is diminished by the length of data necessary to make robust estimates of the narrowband phase shifts and the rate at which the phase shifts change over the signal wavetrain. We recommend using the matched field traces to confirm the presence of a signal of interest and subsequently using the AR-AIC trace for an optimal estimate of the phase arrival time.

A number of signals at the noise level in the plane-wave matched field detection trace are elevated to clear detections in the empirical matched field detection trace. This is primarily a result of the phase shifts changing to match the observed wavefield as a function of frequency and therefore compensating for the deformation of the wavefield observed. We know from the differences between the plane-wave and empirical steering vectors (Fig. 5) that waveform misalignment will occur at the higher frequencies if the plane-wave time-shifts are applied. We also know (Fig. 2) that the smaller events are only well observed above the coda noise at these frequencies. An observation that was not obvious prior to the study is that the phase shifts measured from the mainshock first arrival would also be applicable to the vast majority of events in the aftershock zone (see Figs. 6 and 7).

We note that each of the matched field traces displayed in Fig. 12 c) is generated by a single steering vector. It may be sufficient when tracking an aftershock sequence to have a single template (e.g. the first arrival from the mainshock) on each array being used, and there are clear operational advantages to restricting the process to a single steering vector. Whether additional matched field templates from subsequent aftershocks would significantly improve aftershock recovery rates, or simply provide duplication of effort, would need to be investigated empirically. The answer to this question would depend upon the size of the aftershock zone and the relative location and properties of the observing array. An exceptionally large aftershock zone may necessitate multiple templates aimed at different parts of the aftershock region. The templates in this paper have been exclusively initial P-arrivals from the main shock at each array. The procedure could be extended to use different templates for different phases in the wavetrain at a given station, for example Pn, Pg, Sn, Lg, P, and S as appropriate, in order to increase the sensitivity. Köhler et al. (2022), for example, used an empirical steering vector of an S-wave template in addition to the P-wave template to detect repeating events at a calving glacier in Svalbard, mainly to compensate for the lack of multiple array observations. This could be applied without difficulty in that study given the very limited geographical extent of the source region; a single S-P time-delay was applicable to the entire zone of glacial calving. For an extended aftershock zone, the time-offsets between the different phases in single wavetrains would need to be accounted for. The

restriction to the initial P-arrival from the mainshock is advantageous for a semi-autonomous procedure. Any extension of the method that requires secondary phases for matched field templates will demand additional human interaction and supervision. Given an observational network with multiple arrays, using secondary phases may be both unnecessary and detrimental to performance.

5 CONCLUSIONS

We wish to characterize aftershock sequences as accurately as possible using automatic signal processing in order to reduce the human effort of compiling comprehensive seismic event bulletins. The classical processing pipeline of single-station phase detection, followed by global phase association, frequently breaks down under extensive aftershock sequences due to the vast number of detections and limitations in current algorithms for building events. Correlation and subspace detectors show promise for building event lists for many categories of aftershock sequences. However, for the largest sequences, the full-waveform signal detectors often perform poorly due to large inter-event distances, differences in spectral properties, and differences in source mechanism.

We advocate the use of matched field detectors on array stations, using templates constructed from the first P-arrivals from the mainshock, to detect and identify aftershocks reliably. Empirical Matched Field Processing (EMFP) is a pattern detector that recognizes phase patterns in the wavefronts incident on an array, although we here apply it as a single-phase detector analogous to beams used in classical array processing. The deviations from the plane-wavefront model often observed on seismic arrays can be very frequency-dependent and the narrowband wavefield representation of EMFP allows optimal steering over a wide range of discrete frequencies.

Using the aftershock sequence of the October 8, 2005, Kashmir earthquake as an example, we describe many of the complications arising in existing pipelines and demonstrate how EMFP helps to mitigate them. Three clear complications can be listed:

(i) There can be significant deviations from the plane-wavefront model. EMFP mitigates this by calculating empirical and frequency-dependent phase-shifts.

(ii) There is often dominant energy at frequencies higher than those amenable to classical beamforming. (This is particularly an issue for the smaller aftershocks for which the SNR at low frequencies is diminished.) EMFP mitigates this by extending the frequency range at which coherent array-processing can be performed.

(iii) The spectral content of signals from different events in the sequence varies greatly. (This affects both the classical beamforming gain and the bias in direction estimates using f-k analysis.) EMFP mitigates this with a frequency-by-frequency approach that recognizes coherence between array elements

at all frequencies where it is observed, and that diminishes the influence of frequencies where the signals are excessively incoherent or poorly observed.

The process described for tracking aftershock sequences can be applied to multiple stations in a regional or global network. When applying the methodology presented here to four large aftershock sequences using data from stations of the International Monitoring System of the CTBTO, the conference presentation Köhler et al. (2020) demonstrated that about 50% of the verified aftershocks could be automatically detected and located with high accuracy. A general grid search methodology was used for associating the EMFP phase detections at the different stations (e.g. Gibbons et al. 2016). The parametric data that can be obtained using the methods described in this paper can facilitate far more advanced association models (e.g. Arora et al. 2013; Le Bras et al. 2021), which again could provide improved aftershock processing results.

Significant progress has been made using waveform similarity for aftershock processing and more general seismic pipelines (e.g. Harris & Dodge 2011; Junek et al. 2015; Dodge & Harris 2016) and we are now likely entering the phase in which pattern recognition and deep learning algorithms will start to take a dominant role in seismic signal detection and interpretation, both regionally and globally (e.g. Mousavi et al. 2019; Shen et al. 2019; Mousavi & Beroza 2022). Empirical Matched Field Processing exploits features of the seismic wavefield at array stations that are more characteristic than the shapes of the waveforms themselves and will likely make a contribution to future as well as current seismic processing pipelines.

ACKNOWLEDGMENTS

This work was partly supported by the Air Force Research Laboratory under contract FA9453-16-C-0006. The authors would like to thank Joshua Carmichael and an anonymous reviewer for their careful reading of our manuscript and insightful comments that helped improve the manuscript. Most maps and figures in this paper are created using GMT software (Wessel & Smith 1995). The elements of the covariance matrices were calculated using the FORTRAN90 multitaper routines written by German Prieto (see Prieto et al. 2009) and can be obtained from `https://www.gaprieto.com/software/` (last accessed April 2023). Readers may be interested to know that there is now a Python implementation of the multitaper routines (Prieto 2022) available at `https://github.com/gaprieto/multitaper` (last accessed April 2023) although these were not used in the current paper.

DATA AVAILABILITY

The data from the KKAR-array is available from via the Seismological Facility for the Advancement of Geoscience operated by the EarthScope Consortium at `https://ds.iris.edu/ds/nodes/dmc/data/` (network KZ, last accessed April 2023).

REFERENCES

Arora, N. S., Russell, S., & Sudderth, E., 2013, NET-VISA: Network processing vertically integrated seismic analysis, *Bulletin of the Seismological Society of America*, **103**(2A), 709–729.

Benz, H. M., McMahon, N. D., Aster, R. C., McNamara, D. E., & Harris, D. B., 2015, Hundreds of earthquakes per day: The 2014 Guthrie, Oklahoma, earthquake sequence, *Seismological Research Letters*, **86**, 1318–1325.

Butler, R. W. H., 2019, Tectonic evolution of the Himalayan syntaxes: the view from Nanga Parbat, *Geological Society, London, Special Publications*, **483**, 215–254.

Dodge, D. A. & Harris, D. B., 2016, Large-scale test of dynamic correlation processors: Implications for correlation-based seismic pipelines, *Bulletin of the Seismological Society of America*, **106**, 435–452.

Gibbons, S. J., 2014, The Applicability of Incoherent Array Processing to IMS Seismic Arrays, *Pure and Applied Geophysics*, **171**, 377–394.

Gibbons, S. J. & Kværna, T., 2017, Illuminating the seismicity pattern of the October 8, 2005, M = 7.6 Kashmir earthquake aftershocks, *Physics of the Earth and Planetary Interiors*, **270**, 1–8.

Gibbons, S. J., Ringdal, F., & Kværna, T., 2008, Detection and characterization of seismic phases using continuous spectral estimation on incoherent and partially coherent arrays, *Geophysical Journal International*, **172**(1), 405–421.

Gibbons, S. J., Kværna, T., Harris, D. B., & Dodge, D. A., 2016, Iterative strategies for aftershock classification in automatic seismic processing pipelines, *Seismological Research Letters*, **87**(4), 919–929.

Gibbons, S. J., Harris, D. B., Dahl-Jensen, T., Kværna, T., Larsen, T. B., Paulsen, B., & Voss, P. H., 2017, Locating seismicity on the Arctic plate boundary using multiple-event techniques and empirical signal processing, *Geophysical Journal International*, **211**(3), 1613–1627.

Harris, D. B. & Dodge, D. A., 2011, An autonomous system for grouping events in a developing aftershock sequence, *Bulletin of the Seismological Society of America*, **101**, 763–774.

Harris, D. B. & Kværna, T., 2010, Superresolution with seismic arrays using Empirical Matched Field Processing, *Geophys. J. Int.*, **182**, 1455–1477, doi:10.1111/j.1365-246X.2010.04684.x.

Johnson, D. H. & Dudgeon, D. E., 1993, *Array signal processing: concepts and techniques*, Prentice Hall.

Joswig, M., 1990, Pattern recognition for earthquake detection, *Bull. Seism. Soc. Am.*, **80**, 170–186.

Junek, W. N., Kværna, T., Pirli, M., Schweitzer, J., Harris, D. B., Dodge, D. A., & Woods, M. T., 2015, Inferring aftershock sequence properties and tectonic structure using empirical signal detectors, *Pure and Applied Geophysics*, **172**, 359–373.

Köhler, A., Kværna, T., & Gibbons, S. J., 2020, Assessment of the empirical matched field processing algorithm

for autonomous tracking of aftershock sequences, in *EGU General Assembly 2020, Online, 4–8 May, EGU2020-9396*, Copernicus GmbH.

Köhler, A., Myklebust, E. B., & Mæland, S., 2022, Enhancing seismic calving event identification in Svalbard through empirical matched field processing and machine learning, *Geophysical Journal International*, **230**(2), 1305–1317.

Kværna, T. & Doornbos, D. J., 1991, Scattering of regional Pn by moho topography, *Geophys. Res. Lett.*, **18**, 1273–1276, doi:10.1029/91GL01292.

Kværna, T., Gibbons, S. J., & Näsholm, S. P., 2021, CTBT seismic monitoring using coherent and incoherent array processing, *Journal of Seismology*, **25**(5), 1189–1207.

Le Bras, R., Arora, N., Kushida, N., Mialle, P., Bondar, I., Tomuta, E., Alamneh, F. K., Feitio, P., Villarroel, M., Vera, B., Sudakov, A., Laban, S., Nippress, S., Bowers, D., Russell, S., & Taylor, T., 2021, NET-VISA from cradle to adulthood. A machine-learning tool for seismo-acoustic automatic association, *Pure and Applied Geophysics*, **178**, 2437–2458.

Mousavi, S. M. & Beroza, G. C., 2022, Machine learning in earthquake seismology, *Annual Review of Earth and Planetary Sciences*, **51**.

Mousavi, S. M., Sheng, Y., Zhu, W., & Beroza, G. C., 2019, STanford EArthquake Dataset (STEAD): A global data set of seismic signals for AI, *IEEE Access*, **7**, 179464–179476.

Prieto, G. A., 2022, The multitaper spectrum analysis package in Python, *Seismological Research Letters*, **93**, 1922–1929.

Prieto, G. A., Parker, R. L., & Vernon, F. L., 2009, A Fortran 90 library for multitaper spectrum analysis, *Computers & Geosciences*, **35**, 1701–1710.

Ringdal, F., Harris, D. B., Kværna, T., & Gibbons, S. J., 2009, Expanding coherent array processing to larger apertures using Empirical Matched Field Processing, in *Proceedings of the 2009 Monitoring Research Review: Ground-Based Nuclear Explosion Monitoring Technologies" held 21-23 September, 2009 in Tucson, Arizona, doi:10.6084/m9.figshare.14865342.v1*, pp. 379–388.

Sanborn, C. J. & Cormier, V. F., 2018, Modelling the blockage of Lg waves from three-dimensional variations in crustal structure, *Geophysical Journal International*, **214**(2), 1426–1440.

Shen, D., Zhang, Q., Xu, T., Zhu, H., Zhao, W., Yin, Z., Zhou, P., Fang, L., Chen, E., & Xiong, H., 2019, Machine Learning-enhanced Realistic Framework for Real-time Seismic Monitoring – The Winning Solution of the 2017 International Aftershock Detection Contest, *arXiv*, pp. 1–19.

Slinkard, M. E., Carr, D. B., & Young, C. J., 2013, Applying Waveform Correlation to Three Aftershock Sequences, *Bulletin of the Seismological Society of America*, **103**, 675–693.

Tang, C.-C., Lin, C.-H., & Peng, Z., 2014, Spatial-temporal evolution of early aftershocks following the 2010 ML 6.4 Jiashian earthquake in southern Taiwan, *Geophysical Journal International*, **199**(3), 1772–1783.

Taylor, S. R., Arrowsmith, S. J., & Anderson, D. N., 2010, Detection of short time transients from spectrograms using scan statistics, *Bull. Seism. Soc. Am.*, **100**(5A), 1940–1951.

Thomson, D. J., 1982, Spectrum estimation and harmonic analysis, *Proc. IEEE*, **70**(9), 1055–1096.

Wang, J., Templeton, D. C., & Harris, D. B., 2015, Discovering new events beyond the catalogue: application of empirical matched field processing to Salton Sea geothermal field seismicity, *Geophysical Journal International*, **203**(1), 22–32.

Wessel, P. & Smith, W. H. F., 1995, New version of the Generic Mapping Tools, *EOS Trans. Am. Geophys. Union*, **76**, 329.

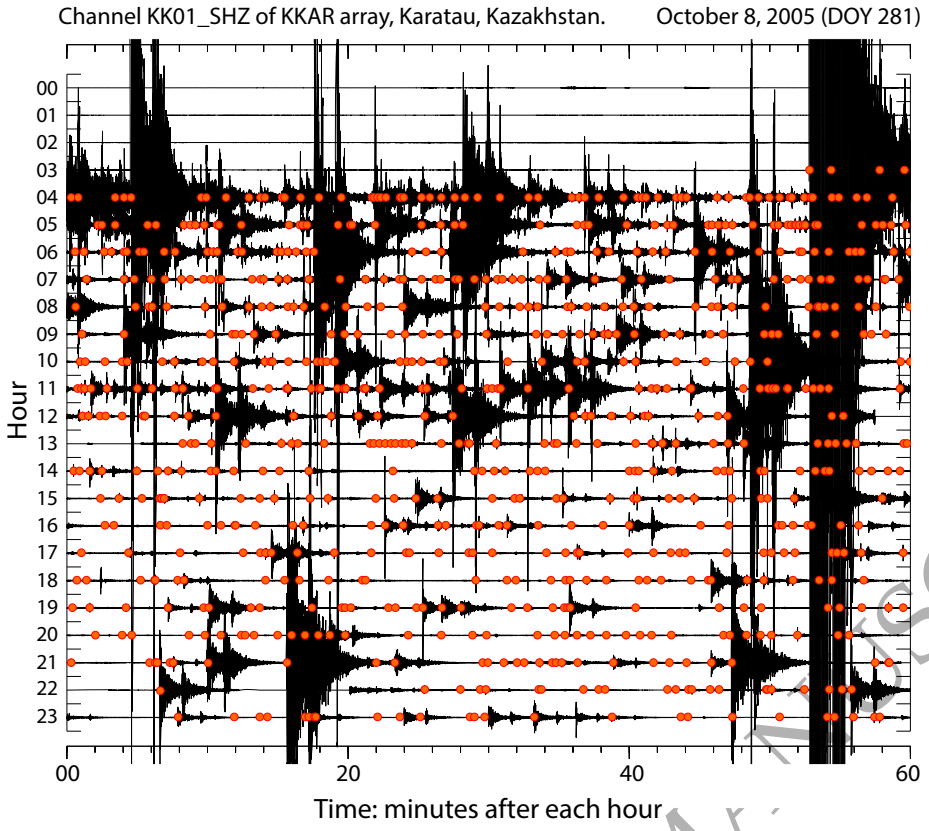

Figure 1. A dayplot of waveform data, bandpass filtered 2-8 Hz, from the KK01 SHZ element of the Karatau array (KKAR) on October 8, 2005. The red symbols indicate detections for which array analysis ($f-k$ analysis) returned an apparent velocity in the interval $7-10$ km/s and a backazimuth between 150 and 175 degrees, corresponding to Pn phases from the aftershock region of the magnitude 7.6 Kashmir earthquake. The $f-k$ analyses were performed in the fixed frequency band $2-4$ Hz, in a 3.5 second time window starting at the signal onset determined by the autoregressive AR-AIC method. Notice the lack of signal detections (red symbols) within the wavetrains of the larger earthquakes. Smaller earthquakes in these time intervals are masked by the phase arrivals and associated coda of the larger events. KKAR consists of 9 vertical component sensors deployed in two concentric circles with approximate radii of 500 meters and 2000 meters, respectively. The geometry of the KKAR is shown in Fig. 3.

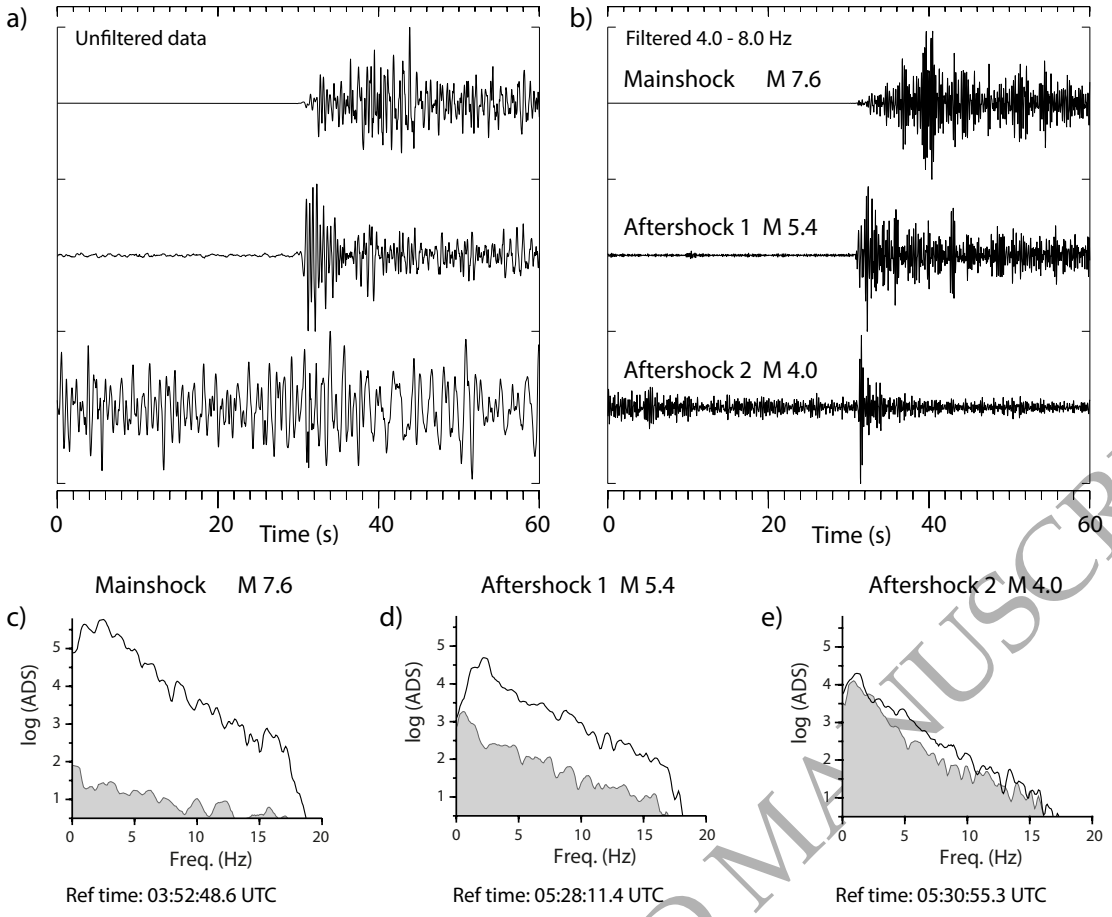

Figure 2. Signals on the KKAR array from 3 events in the Kashmir earthquake sequence recorded on October 8, 2005. Waveforms from the channel KK01 SHZ are displayed centered on three Pn arrivals in panels a) (unfiltered) and b) (bandpass filtered, $4 - 8$ Hz). The times of the arrivals are specified in the spectrum estimates in panels c), d) and e) for which a multitaper estimate (Thomson 1982) of the amplitude density spectrum (ADS) is calculated for 10-second windows for the signal arrival (black line) and the preceding noise (grey-shaded).

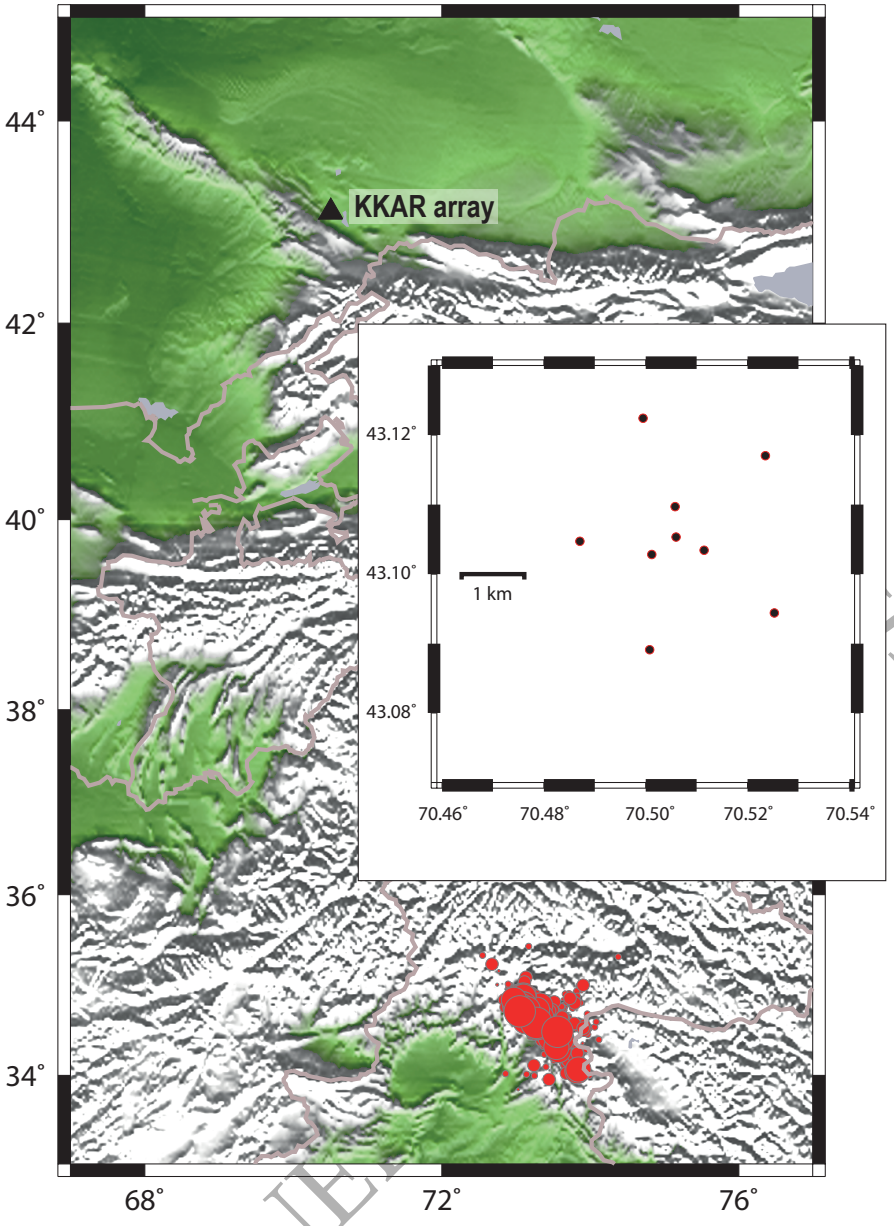

Figure 3. Relocated aftershocks (red filled circles) of the October 8, 2005, Kashmir earthquake in relation to the KKAR array (geometry shown in the inset). The distance from the aftershock region to KKAR is about 900 km.

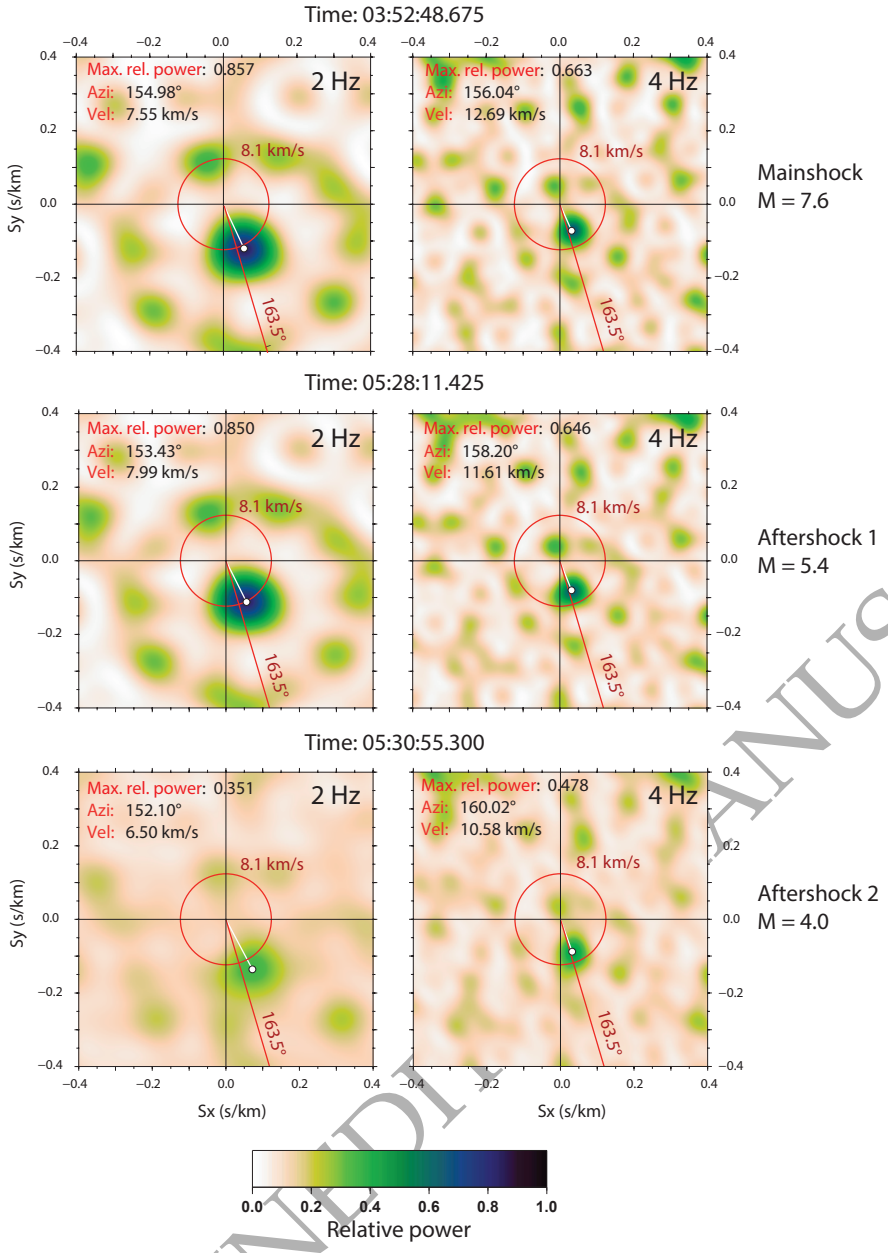

Figure 4. Narrowband $f - k$ analysis at 2 Hz (left) and 4 Hz (right) for the Pn phase arrivals displayed in Fig. 2. The color scale shows relative beam power on the slowness grid with the maximum (the backazimuth and apparent velocity estimate) indicated by the filled white circular symbol. The slowness vector corresponding to the maximum relative power is referred to in the text as the optimal slowness vector. The red circle indicates a constant apparent velocity of 8.1 km/s and the red line labelled 163.5° points in the geographical direction of the October 8, 2005, Kashmir main shock. Notice the differences in backazimuth and apparent velocities when estimated at 2 Hz and 4 Hz, respectively, as well as the similarity between the events at a particular frequency. The frequencies between 2 and 4 Hz (not shown) indicate a progression from one pattern to the other, with the peak narrowing and the relative strength of the sidelobes increasing with increasing frequency. Above 4 Hz, the ability to discern a clear direction of the incoming wavefield diminishes as the combined effects of aliasing and signal incoherence make the main lobe indistinguishable from the multiple sidelobes.

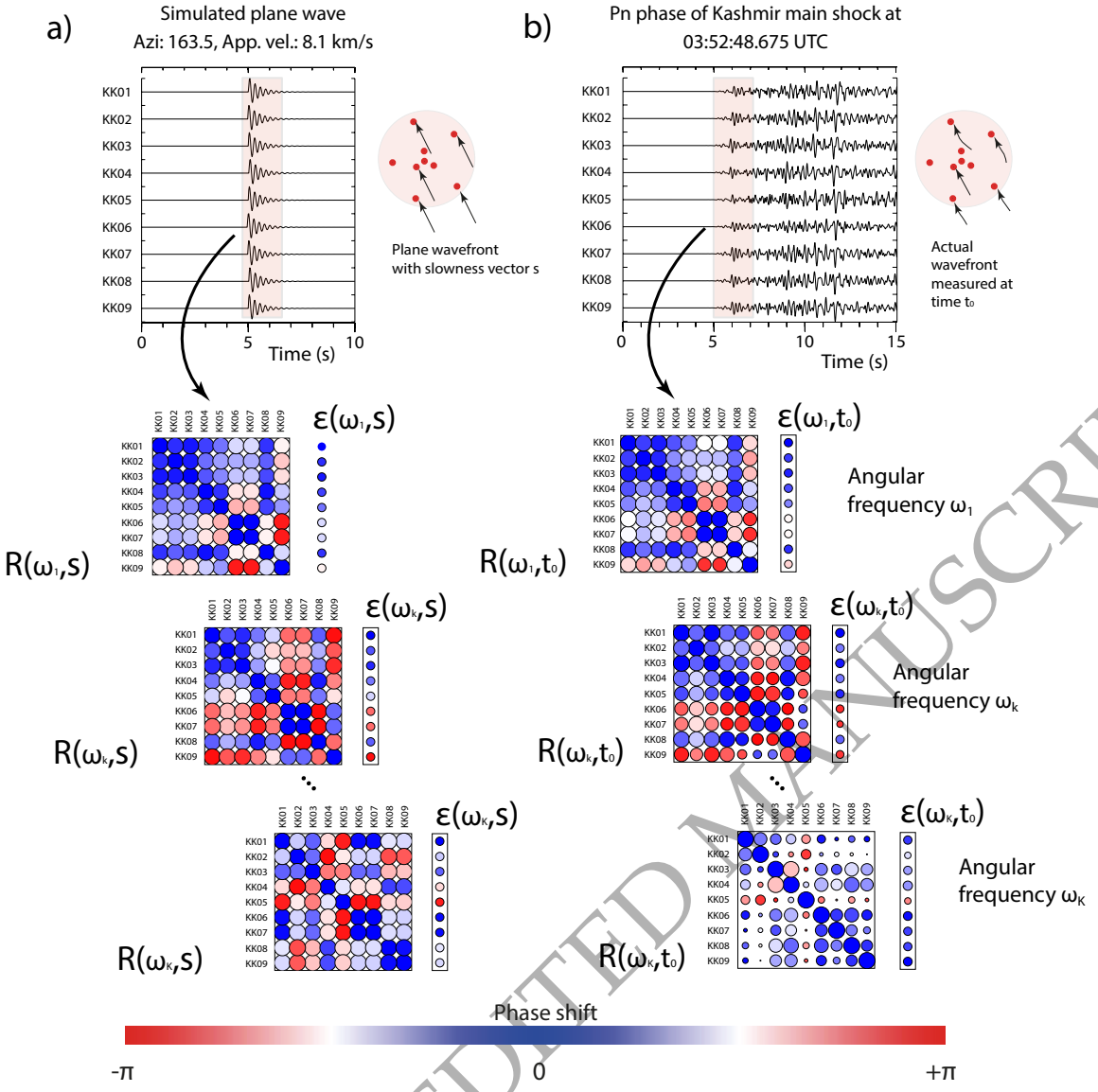

Figure 5. Covariance matrices and empirical steering vectors from KKAR array data for a) a simulated perfect plane wavefront and b) the first P-wave arrival for the Kashmir mainshock. The differences between the theoretical and real-world covariance matrices increase with increasing frequency. The colours represent the phase shifts at each frequency band. Details in text.

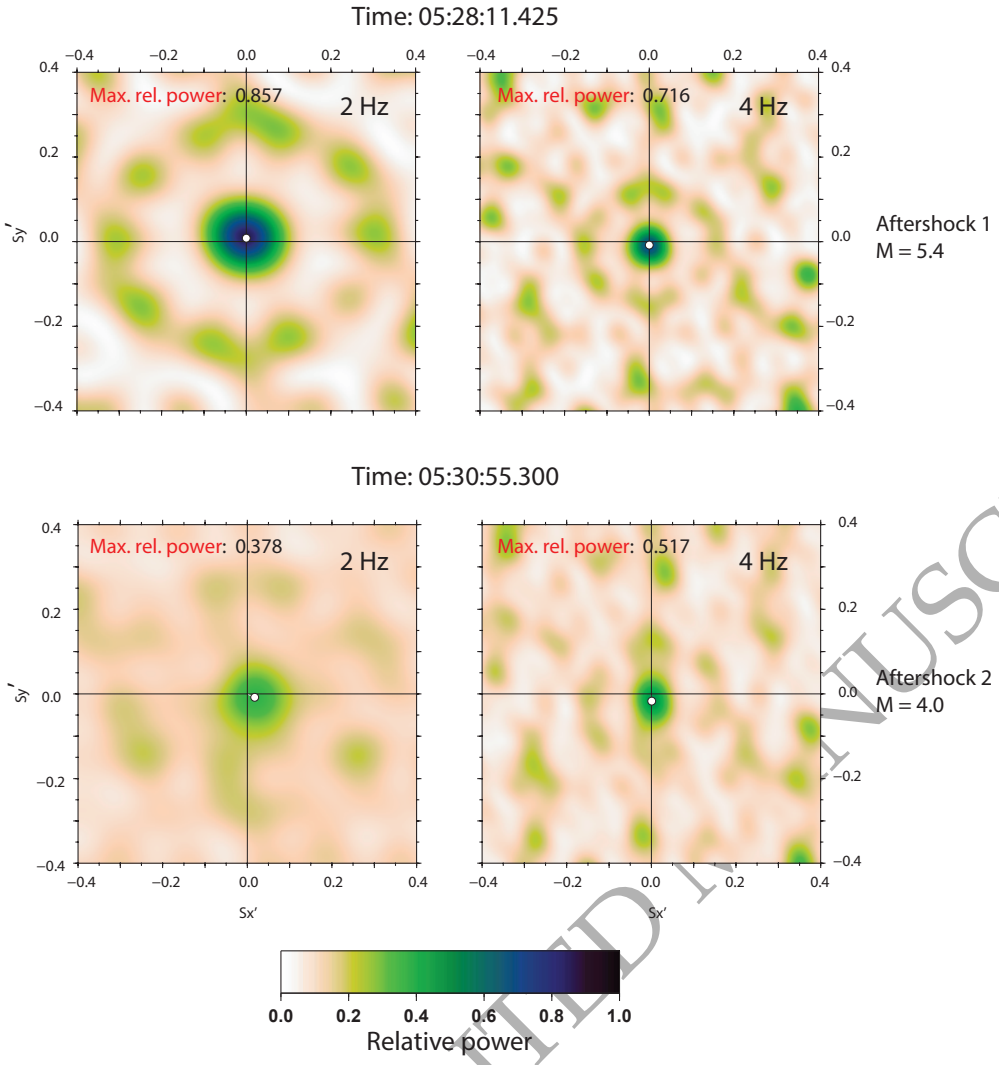

Figure 6. Narrowband $f-k$ analysis at 2 Hz (left) and 4 Hz (right) for the Pn phase arrivals for the two aftershocks (see Fig. 2) relative to the imposed empirical steering vector calculated for the mainshock Pn arrival (c.f. Eq. 5). The arrival times for the two aftershocks, both occurring on 8 October, 2005, are given in the figure. The panels visualize the sensitivity of the EMFP beam power to a changing source location. High power at zero slowness means that a small variation in source location in the aftershock region does not have a significant impact on the EMFP results. We can say that the array is not able to resolve a difference between the directions of arrival for the three events. Whereas estimating the slowness vector using classical plane-wave $f-k$ analysis will give a different result depending upon the frequency band (Fig. 4), the zero-slowness vector relative estimates displayed here appear stable over different frequency bands.

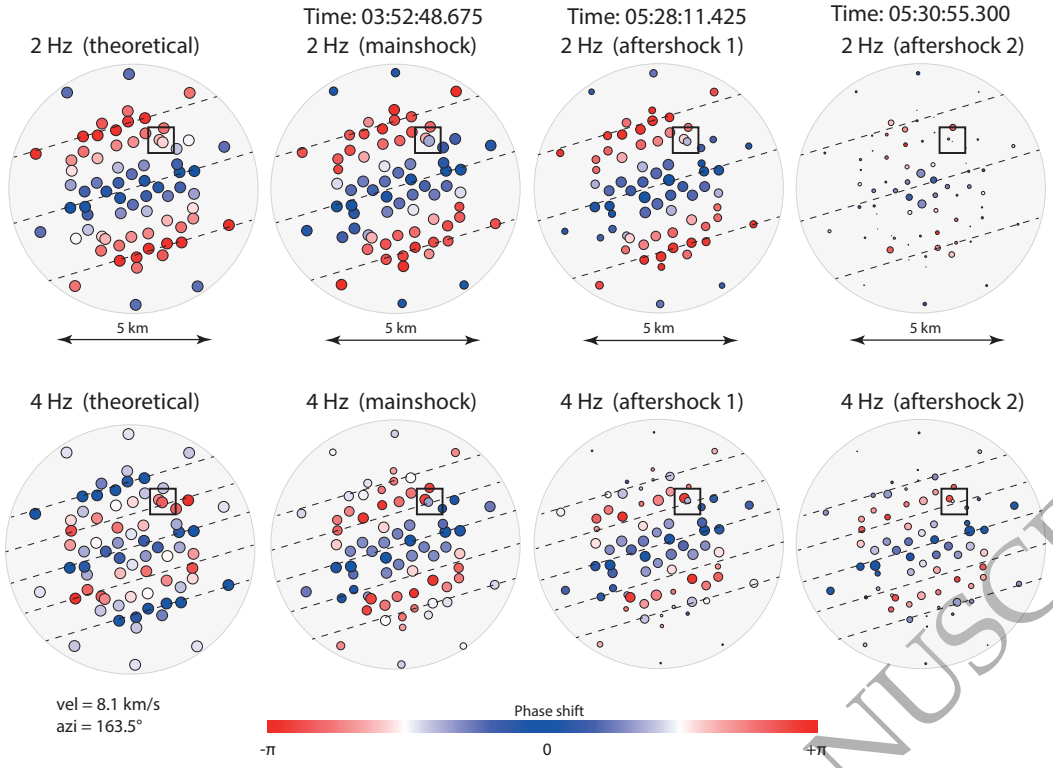

Figure 7. Bubble plots for the KKAR array at 2 Hz and 4 Hz for a theoretical plane-wave arrival from the location of the Kashmir mainshock and for the empirically measured phase shifts for the three events on October 8, 2005, as indicated (see waveforms in Fig. 2). The dashed lines represent wavefronts, separated with a half wavelength, arriving at the array with an apparent velocity of 8.1 km/s and a backazimuth of 163.5°. The reference times for "mainshock", "aftershock 1", and "aftershock 2" are given above the upper panels. The small black box in the different panels highlights two points in the co-array with almost identical locations. The phase differences are indicated in colour and the circle diameters are proportional to coherence.

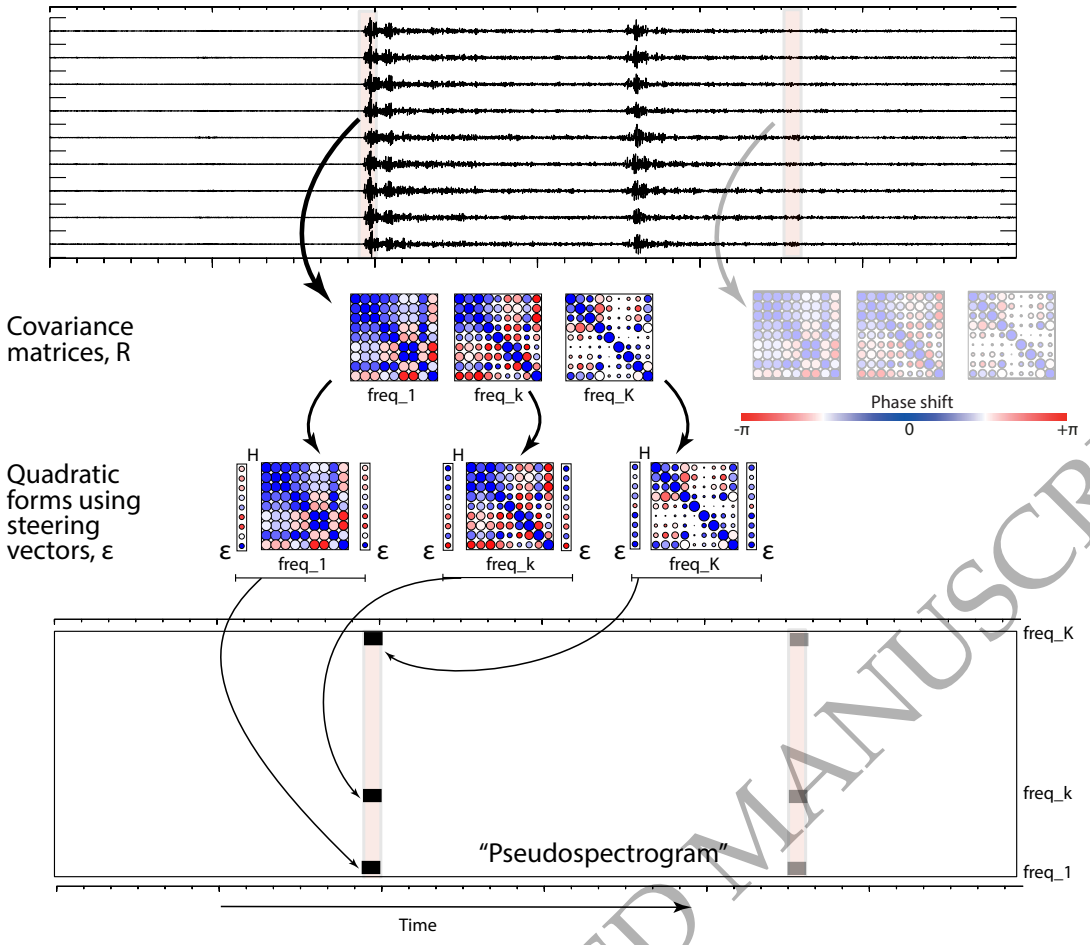

Figure 8. A sketch illustrating the generation of a matched field pseudospectrogram from a single seismic array. For short overlapping time windows, the array covariance matrix is computed for different narrow filter bands. Multiplication with empirical steering vectors of the main shock results in beam power for different frequencies according to Eq. 4. The colors and size of the elements of the covariance matrices $\boldsymbol{R}$ represent, respectively, the relative phase shift and the coherency between the array sensor pairs. Similarly, the colors and size of the steering vectors $\boldsymbol{\varepsilon}$ correspond to the phase and amplitude.

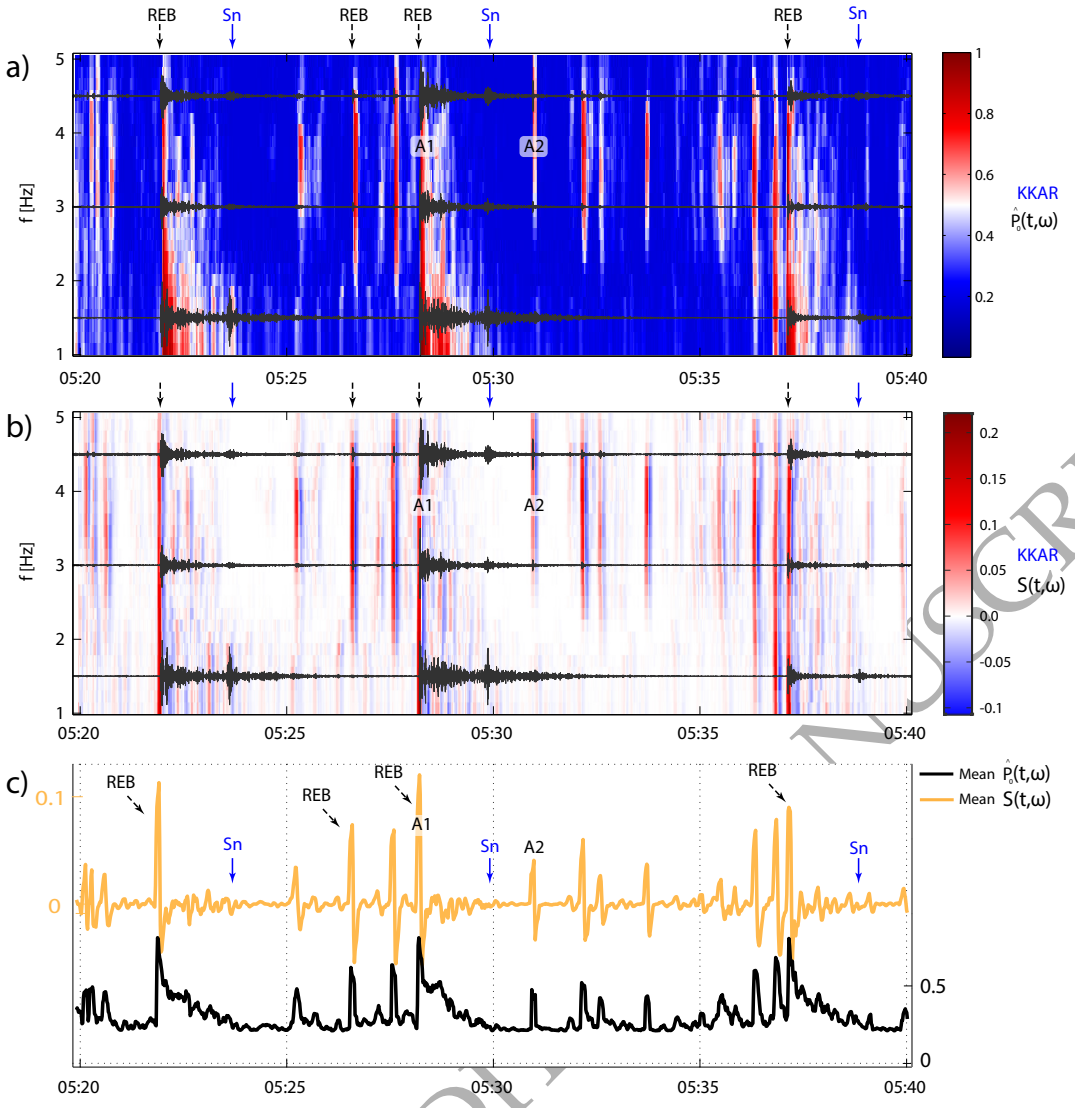

Figure 9. Panel a) shows the pseudospectrogram $\hat{P}_0(t,\omega)$, i.e., beam power for narrow frequency bands and short overlapping time windows using the empirical steering vector of the main shock, for a 20 minute segment of KKAR data on October 8, 2005. The waveforms centered on 1.5, 3, and 4.5 Hz display the plane-wave KKAR Pn beam steered towards the source region, band-pass filtered at the center frequencies indicated with bandwidth 1 Hz. Blue pixels indicate times and frequencies with little energy incident on the array consistent with the phase shifts in the empirical steering vector; red pixels indicate that incident energy is dominated by a wavefront consistent with this phase pattern. Panel b) shows $S(t,\omega)$, a transformation of $\hat{P}_0(t,\omega)$ enhancing changes in consistency with the template steering vector. Panel c) shows a black line for beam power $\hat{P}_0(t,\omega)$ averaged over all frequencies of the top panel. Similarly, the orange line is frequency average of the $S(t,\omega)$ of the middle panel as a function of time. The time of the P-arrivals from the two aftershocks displayed in Fig. 2 are labelled "A1" and "A2", respectively. The dashed black arrows correspond to Pn signals from the four aftershocks reported during this time interval in the REB. The solid blue arrows indicate Sn arrivals from the three largest aftershocks in the time window. Notice that these Sn arrivals are efficiently suppressed by the EMFP processing procedure.

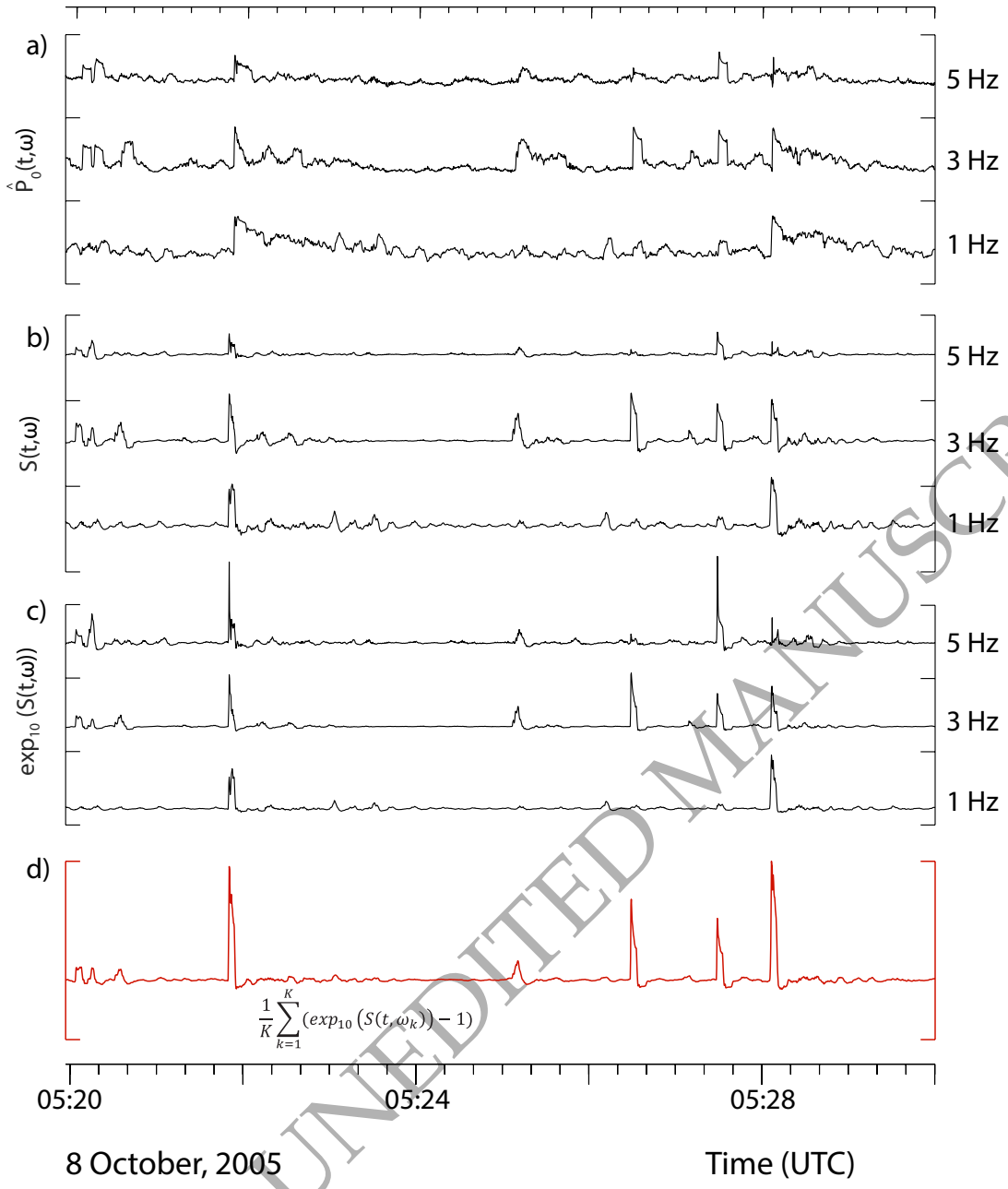

Figure 10. Generation of a robust detection statistic from matched field pseudospectrograms. Panels (a) and (b) display the functions in panels (a) and (b) of Fig. 9 for three discrete frequencies. Panel (c) shows the exponential of the scalar functions in panel (b) and (d) shows the mean over ω of the functions in (c).

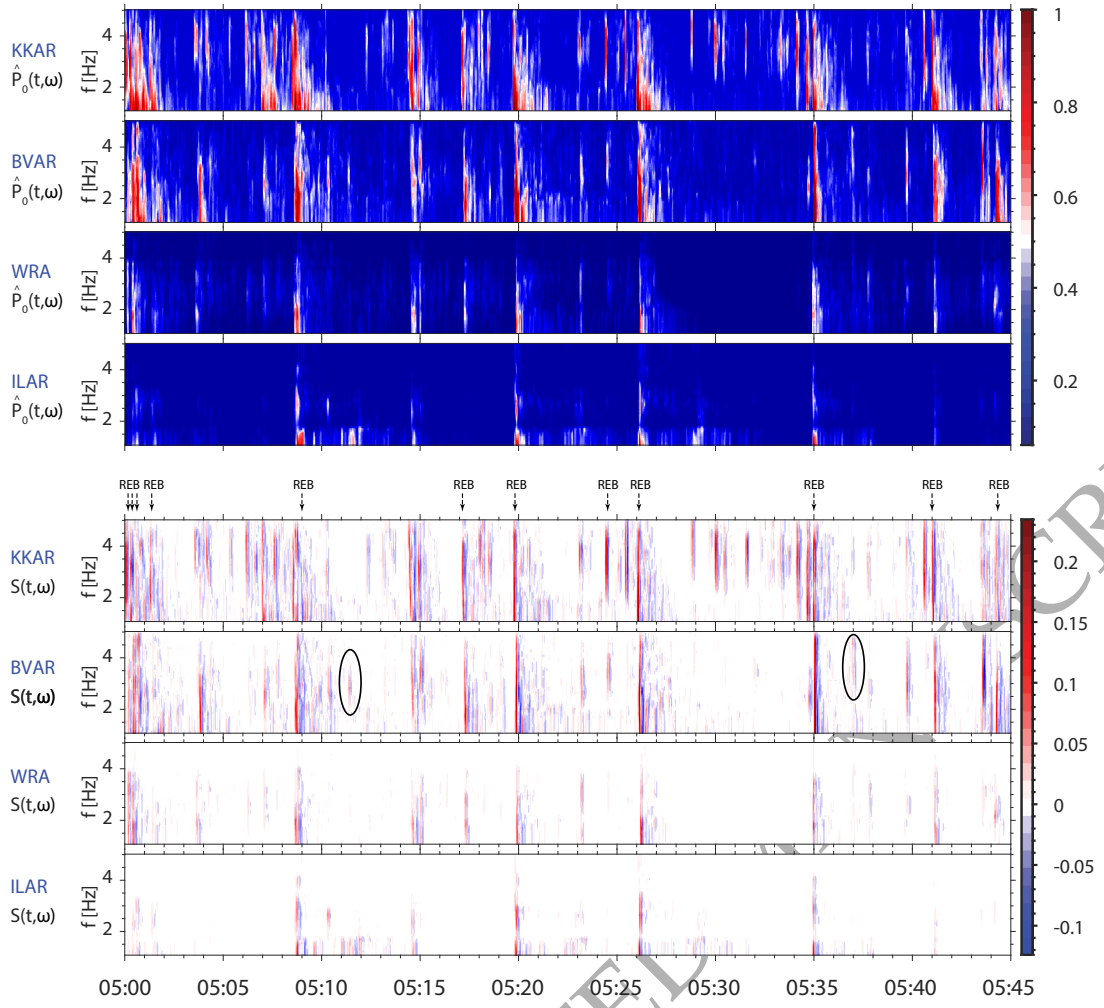

Figure 11. Pseudospectrograms for the KKAR, BVAR, WRA, and ILAR arrays on October 8, 2005. Distances from the Kashmir mainshock are 9 degrees (KKAR, Kazakhstan), 19 degrees (BVAR, Kazakhstan), 80 degreees (WRA, Australia), and 76 degrees (ILAR, Alaska, USA). The $\hat{P}(t,\omega)$ and $S(t,\omega)$ pseudospectrograms have been shifted according to the traveltimes from the mainshock to the different stations. The vertical dashed arrows correspond to aftershocks reported in the REB. Notice that there are several instances of concurrent vertical red stripes across the different $S(t,\omega)$ pseudospectrograms which are not associated with any REB events. These instances correspond to P-arrivals from additional aftershocks. The black ovals indicate EMFP detections at BVAR that are likely to correspond to events in the sequence for which the Pn arrival at KKAR is obscured by coda-wave energy from earlier events.

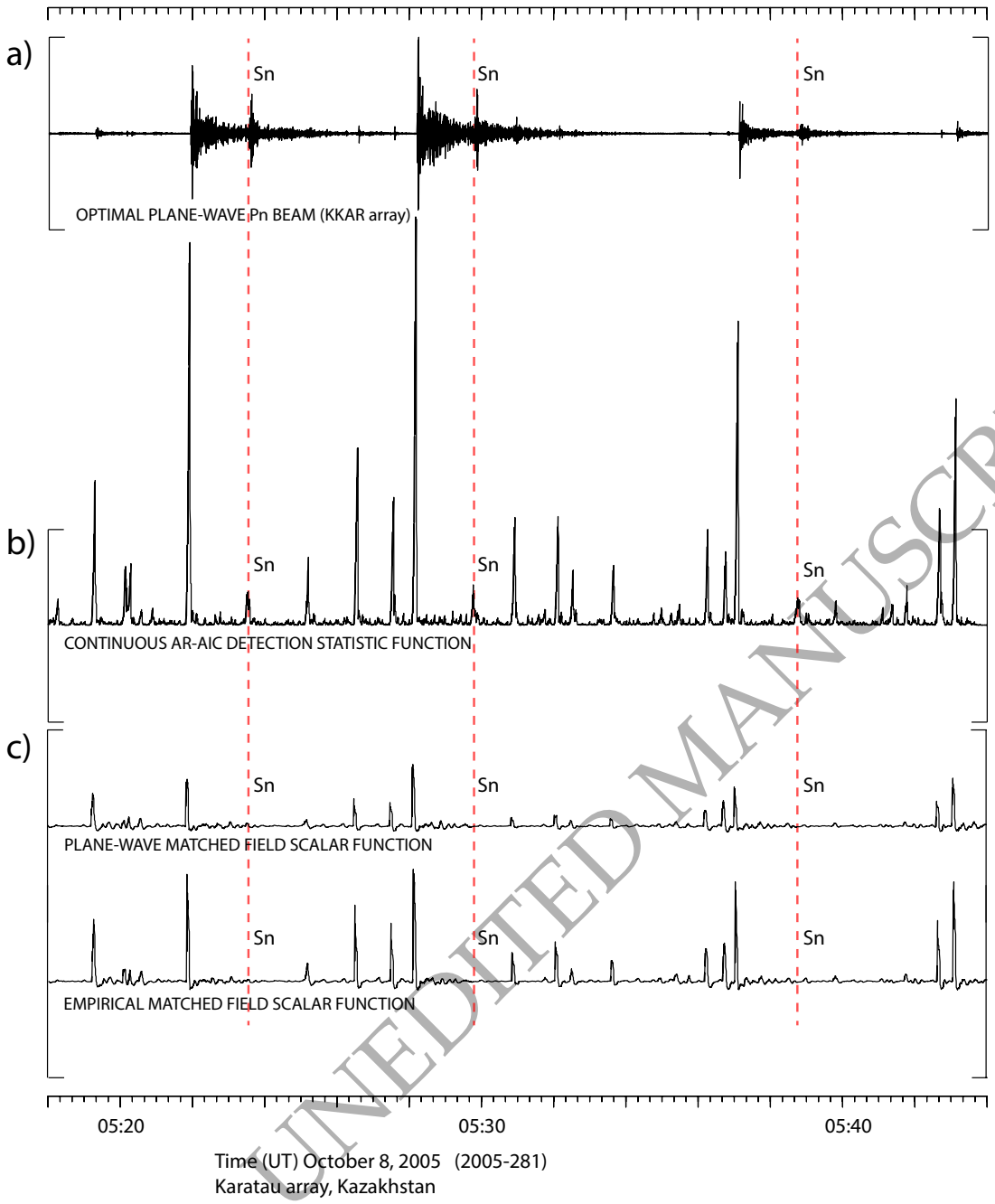

Figure 12. Detection statistics for identifying Pn arrivals from Kashmir earthquake aftershocks on the KKAR array. a) shows the optimized plane-wave Pn beam, bandpass filtered 1-5 Hz, b) shows the continuous AR-AIC detection statistic (Gibbons et al. 2016), and c) displays the scalar functions derived (c.f. Fig. 10 d) for two different steering vectors: the plane-wave phase shifts predicted for the Kashmir mainshock and the empirical phase shifts measured from the mainshock first arrival. The two matched field traces in panel c) are displayed with the same vertical scale.